Supplementary information for "Unidirectional Chiral Emission via Twisted Bi-layer Metasurfaces"

Dmitrii Gromyko,[†,‡,@] Shu An,[¶,@] Sergey Gorelik,[§] Jiahui Xu,[‡] Li Jun Lim,[‖] Henry Yit Loong Lee,[¶] Febiana Tjiptoharsono,[¶] Zhi-Kuang Tan,[‖] Cheng-Wei Qiu,[*,‡] Zhaogang Dong,[*,†,¶,⊥] and Lin Wu[*,†,#]

†*Science, Mathematics, and Technology (SMT), Singapore University of Technology and Design (SUTD), 8 Somapah Road, Singapore 487372, Singapore.*

‡*Department of Electrical and Computer Engineering, National University of Singapore, 4 Engineering Drive 3, Singapore 117583, Singapore.*

¶*Institute of Materials Research and Engineering (IMRE), Agency for Science, Technology and Research (A*STAR), 2 Fusionopolis Way, #08-03 Innovis, Singapore 138634, Singapore.*

§*Singapore Institute of Food and Biotechnology Innovation, Agency for Science, Technology and Research (A*STAR), 31 Biopolis Way, #01-02 Nanos, Singapore 138669, Singapore.*

‖*Department of Chemistry, 3 Science Drive 3, National University of Singapore, Singapore 117543, Singapore.*

⊥*Department of Materials Science and Engineering, National University of Singapore, 9 Engineering Drive 1, Singapore 117575, Singapore.*

#*Institute of High Performance Computing, A*STAR (Agency for Science, Technology, and Research), 1 Fusionopolis Way, #16-16 Connexis, Singapore 138632, Singapore.*

@*These authors contributed equally to this work.*

E-mail: chengwei.qiu@nus.edu.sg; zhaogang_dong@sutd.edu.sg; lin_wu@sutd.edu.sg

Contents

Supplementary Note 1. Resonant dipoles formalism 3

Supplementary Note 2. Resonant properties of single-layer metasurfaces of notched discs 5

Supplementary Note 3. Resonant mode coupling for exact chirality conditions 7

Supplementary Note 4. Temporal coupled-mode theory for chiral bi-layer metasurfaces 11

Supplementary Note 5. Comparison of the embedded and open structures for intrinsic chirality 20

Supplementary Note 6. Reflectance spectra for bi-layer metasurfaces operating at unitary background transmission of the Fabry-Pérot type. 23

Supplementary Note 7. Unidirectional resonances in bi-layer metasurfaces with lateral displacement 30

Supplementary Note 8. Extrinsic chirality of configuration D2 32

Supplementary Note 9. Unidirectional chiral emission from configuration D1 34

Supplementary Methods 1. Fabrication 36

Supplementary Methods 2. Optical setup 38

Supplementary Note 1. Resonant dipoles formalism

The interaction of far-field plane waves and resonant modes of periodic photonic structures can be efficiently described using an illustrative model of resonant dipoles. Consider a plane wave with electric field $\mathbf{E}_{\text{inc}}(\omega, \mathbf{r})$ propagating in a medium with background permittivity ε_b that is incident on a structure defined by the permittivity distribution $\varepsilon(\omega, \mathbf{r}) = \varepsilon_b + \Delta\varepsilon(\omega, \mathbf{r})$. The permittivity change $\Delta\varepsilon(\omega, \mathbf{r})$ causes scattering of the incident waves, thus the full electric field is given as a sum of the scattered field and the incident wave:

$$\mathbf{E}(\omega, \mathbf{r}) = \mathbf{E}_{\text{sc}}(\omega, \mathbf{r}) + \mathbf{E}_{\text{inc}}(\omega, \mathbf{r}). \tag{S1}$$

Using the resonant approximation,[1,2] the scattered field is expressed as the sum of the resonant fields $\mathbf{E}_i(\mathbf{r})$ with resonant amplitudes $a_i(\omega)$ that rapidly change in the magnitude and phase in the vicinity of corresponding complex resonant frequencies ω_i and the background term $\tilde{\mathbf{E}}_{\text{sc}}(\omega, \mathbf{r})$ that smoothly varies as a function of frequency. When only one strong resonance determines the structure response, the background term and all distant resonances can be neglected:

$$\mathbf{E}_{\text{sc}}(\omega, \mathbf{r}) = \sum_i a_i(\omega)\mathbf{E}_i(\mathbf{r}) + \tilde{\mathbf{E}}_{\text{sc}}(\omega, \mathbf{r}) \approx \alpha_1(\omega)\mathbf{E}_1(\mathbf{r}). \tag{S2}$$

The resonant amplitude $\alpha_1(\omega)$ is determined using the following formula:

$$\alpha_1(\omega) = -\frac{\omega}{N_1(\omega - \omega_1)} \int_{V_{\text{res}}} \Delta\varepsilon(\omega, \mathbf{r})\mathbf{E}_{\text{inc}}(\omega, \mathbf{r})\mathbf{E}_1(\mathbf{r}) d^3\mathbf{r}, \tag{S3}$$

where N_1 is the normalization constant of the resonant mode with complex frequency ω_1. The integral is taken over the volume V_{res} of the metasurface unit cell. A detailed discussion of the resonant approximation and the resonant mode normalization can be found in Refs.[3,4] Considering a normally incident plane wave $\mathbf{E}_{\text{inc}}(\omega, \mathbf{r}) = \mathbf{E}_0 \exp(ink_0 z)$ to be the excitation

(k_0 is the wavenumber in the free space, n is the refractive index of the embedding medium), one can express the resonant amplitude as a product of the incident wave polarization vector $\mathbf{E}_0$ and a dipole $\mathbf{D}$ that represents the whole resonant mode:

$$\alpha_1(\omega) = -\frac{\omega}{(\omega-\omega_1)}\mathbf{E}_0 \int_{V_{\text{res}}} \frac{\Delta\varepsilon(\omega,\mathbf{r})\exp(ink_0z)\mathbf{E}_1(\mathbf{r})}{N_1} d^3\mathbf{r} = -\frac{\omega}{(\omega-\omega_1)}\mathbf{E}_0\mathbf{D}. \tag{S4}$$

In the main text, we use the ratio of the amplitudes of the same resonant mode excited by normally incident RCP and LCP plane waves to measure the resonance chirality, thus the normalization constant and frequency-dependent terms can be omitted. Moreover, since the thickness of the discs is much smaller than the excitation wavelength, the evaluation of the resonant dipoles can be significantly simplified:

$$\mathbf{D} \approx \int_{V_{\text{disc}}} \mathbf{E}_1(\mathbf{r}) d^3\mathbf{r}. \tag{S5}$$

Supplementary Note 2. Resonant properties of single-layer metasurfaces of notched discs

In this section, we analyze the properties of a single-layer metasurface, which can be either the top or bottom metasurface in the bi-layer metasurface described in the main text. The unit cell of the single-layer metasurface is shown in Supplementary Fig. 1a, it consists of Si discs (the refractive index of silicon is shown in Supplementary Fig. 1b) fully embedded in SiO_2. The structure parameters are: pitch $p = 400$ nm, disc radius $R = 145$ nm, thickness $h = 50$ nm, depth $d = 100$ nm, and width $w = 80$ nm of rectangular notches. Foremost, we consider a periodic array of cylindrical pillars arranged in a square lattice. The structure has D_{4h} symmetry, and all structural parameters are the same as in the main text. All non-degenerate modes of this structure with frequencies lower than the first diffraction opening frequency are BIC at Γ-point (normal light incidence).[5] To make these modes radiative under normal light incidence, a symmetry perturbation should be introduced. We cut rectangular notches in the pillars at angle θ with respect to the y-axis so that the structure symmetry is reduced to C_{1h} (D_{1h} when θ is a multiple of $\pi/4$) (Supplementary Fig. 1a). The four lowest resonant modes for the single-layer metasurface with $\theta = 0$ are shown in (Supplementary Fig. 1c). The reflection spectra under linearly polarized illumination near the first resonant mode at 413 THz are shown in Supplementary Fig. 1d. This quasi-BIC mode arises from the BIC mode that transforms like the A_{2g} irreducible representation of the D_{4h} symmetry group.[6] The sharpest resonant feature is observed for x-polarized waves; for y-polarized waves, on the contrary, no sign of resonant behavior is observed, as coupling this quasi-BIC resonance to a plane wave is proportional to the x-component of the plane wave polarization. The complex reflection amplitude $\hat{r}$ in the vicinity of the resonance for waves with resonance-matching polarization and the nonresonant background term r are shown in Supplementary Fig. 1e. We also apply Eq. (S5) to evaluate the resonant dipoles for different notch angles and specify the selection rules.[5] As shown in Supplementary Fig. 1f, the resonant dipole components

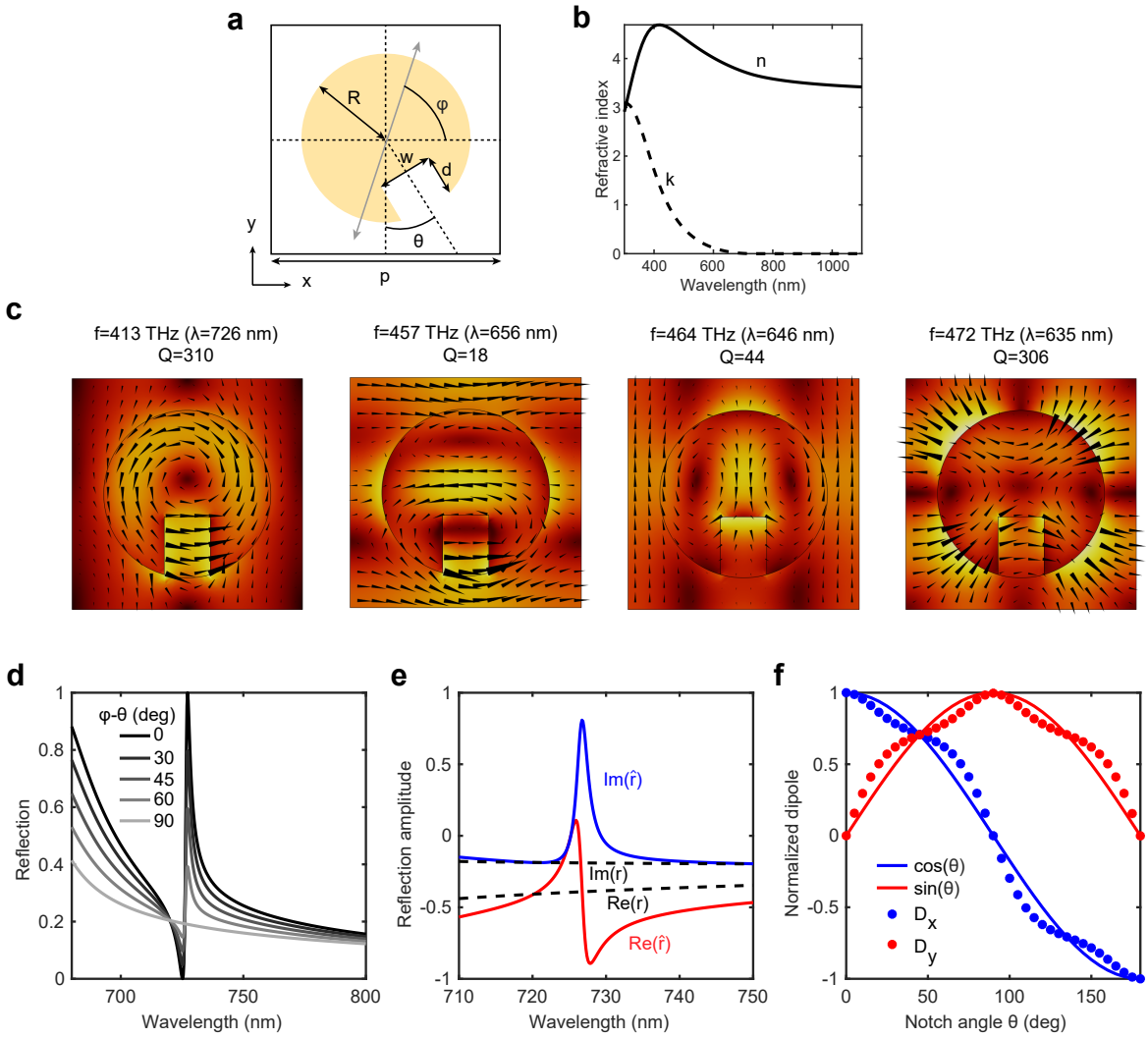

Supplementary Fig. 1: Polarization-selective coupling of the quasi-BIC mode of a single-layer metasurface. **a,** The unit cell of a single-layer metasurface, top view. **b,** Real and imaginary parts of the silicon refractive index. **c,** The electric field profile of the four lowest resonant modes. **d,** Reflection spectra for normally incident plane waves with polarization $\mathbf{E}_0 = (\cos\phi, \sin\phi)$. **e,** Real (red solid line) and imaginary (blue solid line) parts of the amplitude reflection coefficient for plane waves with resonance-matching polarization. Dashed lines indicate real and imaginary parts of the background reflection coefficient r (illumination with resonance-mismatching polarization). **f,** Components of the resonant dipole (D_x, D_y) for the first resonant mode (413 THz) of the single-layer metasurface with different notch angles θ.

approximately follow $\mathbf{D}(\theta) \propto (\cos\theta, \sin\theta)$. Thus, the resonance interaction with plane waves is fully determined by the angle θ: the resonance stays completely decoupled from the waves polarized along the line that connects the notch's center and the disc's center.

Supplementary Note 3. Resonant mode coupling for exact chirality conditions

To provide a rigorous dipole far-field coupling model for the resonant modes of the bi-layer metasurface and derive the absolute intrinsic resonance chirality conditions, we consider two arrays of interlayer-coupled dipoles $\mathbf{D}_1$ separated by distance $H + h$, where h is the single-layer metasurface thickness. First, we approximate the electric fields of the resonant modes in the top and bottom metasurfaces with dipoles:

$$\mathbf{D}_1^{\text{self}} = (\cos\theta, -\sin\theta)\,, \quad \mathbf{D}_2^{\text{self}} = \pm\,(\cos\theta, \sin\theta) \tag{S6}$$

where $\pm$ sign stands for the anti-symmetric and symmetric with mode, respectively. Due to the C_2 symmetry, these dipoles have equal magnitudes and can be normalized to unit length. Secondly, during the coupling process, the excited modes generate evanescent near fields and far-field radiation that induce additional nonresonant electric fields in the counterpart metasurfaces. These induced fields are approximated by the dipoles:

$$\mathbf{D}_1^{\text{ind}} = (C_{\text{nf}}(H) + C_{\text{ff}}e^{-ink_0H})\mathbf{D}_2^{\text{self}}, \quad \mathbf{D}_2^{\text{ind}} = (C_{\text{nf}}(H) + C_{\text{ff}}e^{-ink_0H})\mathbf{D}_1^{\text{self}}, \tag{S7}$$

where C_{ff} is a constant of far-field coupling and $C_{\text{nf}}(H)$ is a term of near-field coupling that quickly decreases in magnitude with interlayer distance H. The resonant dipoles of the coupled modes appear as:

$$\mathbf{D}_n = \mathbf{D}_n^{\text{self}} + \mathbf{D}_n^{\text{ind}} \tag{S8}$$

Next, we show that the far-field coupling coefficient C_{ff} is a background reflection coefficient of a single-layer metasurface. Consider, for example, the bottom metasurface with resonant field approximated by dipole $\mathbf{D}_2^{\text{self}}$. The dipole radiates a plane wave with electric field polarization $C_{\text{rad}}\mathbf{D}_2^{\text{self}}$, where C_{rad} is a proportionality coefficient between the effective

dipole that represents electric fields in a single-layer metasurface and the radiation amplitude. As the radiated wave propagates through the intermediate layer of thickness H and refractive index n it gains a phase factor e^{-ink_0H}. Finally, the wave induces additional nonresonant fields in the top metasurface that are approximated by a dipole $\mathbf{D}_1^{\text{ind}} = e^{-ink_0H} C_{\text{pol}} C_{\text{rad}} \mathbf{D}_2^{\text{self}}$, where C_{pol} is a nonresonant polarizability of a single-layer metasurface.

Now let us consider an isolated single-layer metasurface illuminated by a plane wave of unitary amplitude and polarization $\mathbf{E}_{\text{inc}}$. The nonresonant fields excited in the metasurface can be approximated by an effective dipole $C_{\text{pol}}\mathbf{E}_{\text{inc}}$. In turn, this dipole radiates outgoing plane waves $C_{\text{rad}}C_{\text{pol}}\mathbf{E}_{\text{inc}}$ on the top and bottom boundaries of the metasurface. At the same time, the amplitudes of the nonresonantly scattered waves should be equal to r, thus:

$$C_{\text{ff}} = C_{\text{rad}} C_{\text{pol}} = r, \tag{S9}$$

When an an isolated metasurface is nonresonantly excited by a plane wave, it behaves as a weak symmetric scatterer of thickness h and the scattering amplitudes in the forward and backward directions are both equal to r, so that the transmission coefficient is

$$t = e^{-ink_0h} + r. \tag{S10}$$

We also note that the nonresonant background scattering process is characterized by negligible nonradiative losses; thus, the nonresonant background transmission and reflection coefficients are shifted in phase by $\pi/2$:[7]

$$r = e^{i\Phi}|r|, \quad t = e^{i\Phi} i|t|, \quad |r|^2 + |t|^2 = 1. \tag{S11}$$

According to Eqs. (S7, S8), the resonant dipoles for the anti-symmetric and symmetric

modes can be written as:

$$\mathbf{D}_1 = (D_x, -D_y)\,, \quad \mathbf{D}_2 = \pm\,(D_x, D_y)\,. \tag{S12}$$

Under RCP and LCP waves with electric fields $\mathbf{e}^{R,L} = (1, \pm i)/\sqrt{2}$ and time-dependence $e^{i\omega t}$ normally incident on the bi-layer metasurface from the top, a hybridized resonance is excited with amplitudes:

$$\alpha^{R,L} \propto \mathbf{e}^{R,L} \cdot \mathbf{D}_1 + \mathbf{e}^{R,L} \cdot \mathbf{D}_2 e^{-ink_0(H+h)}. \tag{S13}$$

Under the conditions

$$\cot(nk_0(H+h)/2) = \mp D_y/D_x, \tag{S14}$$

the resonance amplitude $\alpha^{R,L}$ of the anti-symmetric mode excited by either RCP or LCP wave becomes zero. Such resonance becomes completely decoupled from one of the two circular polarizations, which manifests an absolute intrinsic chirality. At the same time, the symmetric mode exhibits absolute chirality when:

$$\tan(nk_0(H+h)/2) = \pm D_y/D_x. \tag{S15}$$

The conditions (S14) and (S15) can be resolved only when the ratio D_y/D_x is a real number. Assuming that one can neglect the near-field coupling, from Eqs. (S7) and (S9), we infer that absolute chirality can be reached when:

$$\text{a) } re^{-ink_0H} = |r|, \text{ b) } re^{-ink_0H} = -|r| \tag{S16}$$

which are conditions for the background Fabry-Pérot resonance of the stacked structure. The top and bottom single-layer metasurfaces characterized by the nonresonant reflection coefficient r and transmission coefficient t form a symmetric Fabry-Pérot resonator with a

total background transmission coefficient:

$$t^{\mathrm{FP}} = \frac{t^2 e^{-ink_0 H}}{1 - r^2 e^{-2ink_0 H}}, \tag{S17}$$

which reaches unitary amplitude when relations (S16) hold. Substituting coupled dipoles for the anti-symmetric mode in form Eq. (S8) into Eq. (S13), we write:

$$\alpha^{R,L} \propto \cos\theta \left(1 + e^{-ik_0 n(H+h)}\right)\left(1 + re^{-ik_0 nH}\right) \mp i \sin\theta \left(1 - e^{-ik_0 n(H+h)}\right)\left(1 - re^{-ik_0 nH}\right). \tag{S18}$$

Using Eqs. (S9)-(S11) one can show that for the bi-layer metasurface operating at Fabry-Pérot unitary background transmission (S16), the twist angles θ that ensure chirality of anti-symmetric mode are:

$$\text{a)}\ \ \pm\tan\theta = \frac{\sqrt{1-|r|^2}}{1-|r|} \ \text{and b)}\ \ \pm\tan\theta = -\frac{\sqrt{1-|r|^2}}{1+|r|} \tag{S19}$$

The $\pm$ sign corresponds to LCP-coupled and RCP-coupled modes, respectively. Note that for the symmetric mode conditions a) and b) in equation (S19) are interchanged. Solutions of the system of Eqs. (S16), (S19) define the parameters of bi-layer metasurfaces with absolute intrinsic chirality. A comparison of the numerically calculated resonance chirality values and those predicted using the analytical dipole coupling model is shown in Supplementary Fig. 2 of the main text.

Supplementary Note 4. Temporal coupled-mode theory for chiral bi-layer metasurfaces

In this section, we show the direct relation between the dipole coupling model, which we use in the main text, and the more rigorous and widely used temporal-coupled mode theory (TCMT)[8] applied to the scattering matrix formalism. We clarify the role of near-field and far-field coupling and justify the far-field approximation for the dipole model.

The scattering properties of a spatially periodic optical structure can be conveniently expressed in terms of the scattering matrix.[7] The scattering matrix determines how the amplitudes $\mathcal{A}_{in}$ of the incoming waves are related to the amplitudes $\mathcal{A}_{out}$ of the outgoing scattered waves:

$$\mathcal{A}_{out} = \mathrm{S}\mathcal{A}_{in}, \quad \mathcal{A}_{out} = \begin{pmatrix} u_1 \\ d_2 \end{pmatrix}, \quad \mathcal{A}_{in} = \begin{pmatrix} d_1 \\ u_2 \end{pmatrix} \tag{S20}$$

Here, d and u represent the amplitudes of downward and upward propagating waves as well as diffracted waves and evanescent Fourier harmonics[9] having tangential wavevectors $\mathbf{k}_{||}^{(i,j)} = \mathbf{k}_{||}^{(0,0)} + \mathbf{G}^{(i,j)}$, with $\mathbf{k}_{||}^{(0,0)} = (k_x, k_y)$ being the tangential wavevector in the main diffraction channel and $\mathbf{G}^{(i,j)}$ representing all possible vectors of the reciprocal lattice of the structure. Subscripts $1, 2$ in Eq. (S20) denote the amplitudes evaluated directly above and below the outer boundaries of the structure.

According to the theory of optical resonances,[4,10] in the vicinity of N resonances of a structure the scattering matrix can be decomposed into a sum of the frequency-smooth background scattering matrix $\tilde{\mathrm{S}}(\omega)$ and N resonant terms:

$$\mathcal{A}_{out} = \left(\tilde{\mathrm{S}}(\omega) + \sum_{n=1}^{N} \frac{|O_n\rangle \langle I_n|}{\omega - \omega_n} \right) \mathcal{A}_{in}. \tag{S21}$$

$\langle I_n|$ and $|O_n\rangle$ are called the resonant input and output vectors; they determine how a par-

ticular resonance with frequency ω_n couples to the incoming and outgoing waves.

The general theory of resonant mode coupling that includes both far-field and near-field interactions is described in a series of works.[10–13] Here, we show how this formalism can be applied to derive the conditions of maximum chirality in the bi-layer metasurface structure. First, we write down the resonant approximation for the scattering matrices of two stacked metasurfaces (see Supplementary Fig. 2):

$$\begin{aligned}
\begin{pmatrix} |u_1\rangle \\ |d_2^{\mathrm{a}}\rangle \end{pmatrix} &= \left[\begin{pmatrix} \tilde{\mathrm{S}}_{ud}^{\mathrm{a}} & \tilde{\mathrm{S}}_{uu}^{\mathrm{a}} \\ \tilde{\mathrm{S}}_{dd}^{\mathrm{a}} & \tilde{\mathrm{S}}_{du}^{\mathrm{a}} \end{pmatrix} + \sum_{n=1}^{N} \begin{pmatrix} |O_{u,n}^{\mathrm{a}}\rangle \\ |O_{d,n}^{\mathrm{a}}\rangle \end{pmatrix} \frac{1}{\omega - \omega_n^{\mathrm{a}}} \begin{pmatrix} \langle I_{d,n}^{\mathrm{a}}| & \langle I_{u,n}^{\mathrm{a}}| \end{pmatrix} \right] \begin{pmatrix} |d_1\rangle \\ |u_2^{\mathrm{a}}\rangle \end{pmatrix}, \\
\begin{pmatrix} |u_2^{\mathrm{b}}\rangle \\ |d_3\rangle \end{pmatrix} &= \left[\begin{pmatrix} \tilde{\mathrm{S}}_{ud}^{\mathrm{b}} & \tilde{\mathrm{S}}_{uu}^{\mathrm{b}} \\ \tilde{\mathrm{S}}_{dd}^{\mathrm{b}} & \tilde{\mathrm{S}}_{du}^{\mathrm{b}} \end{pmatrix} + \sum_{n=1}^{M} \begin{pmatrix} |O_{u,n}^{\mathrm{b}}\rangle \\ |O_{d,n}^{\mathrm{b}}\rangle \end{pmatrix} \frac{1}{\omega - \omega_n^{\mathrm{b}}} \begin{pmatrix} \langle I_{d,n}^{\mathrm{b}}| & \langle I_{u,n}^{\mathrm{b}}| \end{pmatrix} \right] \begin{pmatrix} |d_2^{\mathrm{b}}\rangle \\ |u_3\rangle \end{pmatrix}.
\end{aligned} \tag{S22}$$

Subscripts $1, 2, 3$ indicate the top half-space, intermediate separation layer, and bottom half-space, respectively. We also distinguish the wave amplitudes found infinitesimally below the top metasurface $|d_2^{\mathrm{a}}\rangle, |u_2^{\mathrm{a}}\rangle$ and infinitesimally above the bottom metasurface $|d_2^{\mathrm{b}}\rangle, |u_2^{\mathrm{b}}\rangle$. Since the resonant expansion in this form is written for all Fourier harmonics, both propagating and evanescent, it fully describes the far-field and near-field optical response of a structure. Nevertheless, in some cases, it is reasonable to consider the truncated S-matrices for the far-field waves propagating in open diffraction channels. The resonant approximation for the far-field scattering matrix is also known as TCMT.[8]

For the top and bottom single-layer metasurfaces with notch angles $\mp\theta$, Eq. (S22) appear

in the truncated far-field form as:

$$\begin{pmatrix} u_{1,x} \\ u_{1,y} \\ d^{\mathrm{a}}_{2,x} \\ d^{\mathrm{a}}_{2,y} \end{pmatrix} = \left[\begin{pmatrix} r & 0 & t & 0 \\ 0 & r & 0 & t \\ t & 0 & r & 0 \\ 0 & t & 0 & r \end{pmatrix} + \begin{pmatrix} \cos\theta \\ -\sin\theta \\ \cos\theta \\ -\sin\theta \end{pmatrix} \frac{A^2}{\omega - \omega_1} \begin{pmatrix} \cos\theta \\ -\sin\theta \\ \cos\theta \\ -\sin\theta \end{pmatrix}^T \right] \begin{pmatrix} d_{1,x} \\ d_{1,y} \\ u^{\mathrm{a}}_{2,x} \\ u^{\mathrm{a}}_{2,y} \end{pmatrix},$$

$$\begin{pmatrix} u^{\mathrm{b}}_{2,x} \\ u^{\mathrm{b}}_{2,y} \\ d_{3,x} \\ d_{3,y} \end{pmatrix} = \left[\begin{pmatrix} r & 0 & t & 0 \\ 0 & r & 0 & t \\ t & 0 & r & 0 \\ 0 & t & 0 & r \end{pmatrix} + \begin{pmatrix} \cos\theta \\ \sin\theta \\ \cos\theta \\ \sin\theta \end{pmatrix} \frac{A^2}{\omega - \omega_1} \begin{pmatrix} \cos\theta \\ \sin\theta \\ \cos\theta \\ \sin\theta \end{pmatrix}^T \right] \begin{pmatrix} d^{\mathrm{b}}_{2,x} \\ d^{\mathrm{b}}_{2,y} \\ u_{3,x} \\ u_{3,y} \end{pmatrix}. \tag{S23}$$

Here, we use the resonant approximation with only one resonant mode at frequency ω_1 in each metasurface, moreover, only the main diffraction channel is open for waves to propagate. The subscripts x and y denote the polarization of the waves, r and t are the background reflection and transmission amplitudes of single-layer metasurfaces, and A is a normalization coefficient.

The amplitudes of the waves that propagate between the two metasurfaces are related through the propagation matrix $\mathcal{P}$:

$$u^{\mathrm{a}}_2 = \mathcal{P} u^{\mathrm{b}}_2, \quad d^{\mathrm{b}}_2 = \mathcal{P} d^{\mathrm{a}}_2, \tag{S24}$$

which, in the case of normally propagating plane waves, is just a phase factor:

$$\mathcal{P} = e^{-ik_0 nH} \equiv e^{-i\phi}. \tag{S25}$$

Here, k_0 is the wavenumber in vacuum, and n is the refractive index of the embedding medium.

The resonant energies Ω^{c} of the stacked structure are calculated as the eigenvalues of the

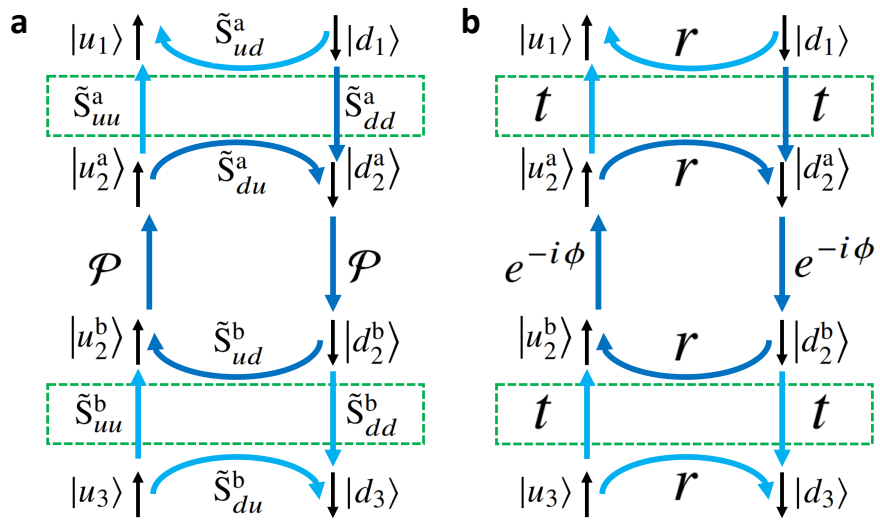

Supplementary Fig. 2: Schematic illustration of the resonant mode coupling. **a,** General approach that includes into consideration both propagating far-field Fourier harmonics and evanescent near-field Fourier harmonics. **b,** TCMT for the system of coupled resonances. Dark blue arrows represent the elements of the subsystems' scattering matrices involved in forming the resonant input vector of the hybridized resonance.

coupling Hamiltonian:[10]

$$\mathcal{H} = \begin{pmatrix} \Omega^{a} + V_{aa} & V_{ab} \\ V_{ba} & \Omega^{b} + V_{bb} \end{pmatrix} = \begin{pmatrix} \Omega^{a} + \left\langle I_u^a \middle| \mathcal{P}\tilde{S}^{b}_{ud}\mathbb{D}_{dd}\mathcal{P} \middle| O_d^a \right\rangle & \langle I_u^a|\mathbb{D}_{uu}\mathcal{P}|O_u^b\rangle \\ \langle I_d^b|\mathbb{D}_{dd}\mathcal{P}|O_d^a\rangle & \Omega^{b} + \left\langle I_d^b \middle| \mathcal{P}\tilde{S}^{a}_{du}\mathbb{D}_{uu}\mathcal{P} \middle| O_u^b \right\rangle \end{pmatrix} \tag{S26}$$

with matrices $\Omega^{a,b} = \mathrm{diag}\{\omega_n^{a,b}\}$ and

$$\mathbb{D}_{dd} = (\mathbb{I} - \mathcal{P}\tilde{S}^{a}_{du}\mathcal{P}\tilde{S}^{b}_{ud})^{-1},\ \mathbb{D}_{uu} = (\mathbb{I} - \mathcal{P}\tilde{S}^{b}_{ud}\mathcal{P}\tilde{S}^{a}_{du})^{-1} \tag{S27}$$

representing the infinite number of internal nonresonant reflections in the Fabry-Pérot cavity formed by the top and bottom subsystems. Due to the C_2 symmetry of the stacked structure, the eigenproblem in the vicinity of the resonant frequency ω_1 can be simplified to the form

of a two-level Hamiltonian with only two independent components:

$$\begin{pmatrix} \omega_1 + V_{\mathrm{aa}} & V_{\mathrm{ab}} \\ V_{\mathrm{ab}} & \omega_1 + V_{\mathrm{aa}} \end{pmatrix} \underbrace{\begin{pmatrix} 1 & 1 \\ 1 & -1 \end{pmatrix}}_{X} = \begin{pmatrix} 1 & 1 \\ 1 & -1 \end{pmatrix} \begin{pmatrix} \omega_A & 0 \\ 0 & \omega_S \end{pmatrix}, \tag{S28}$$

where ω_A and ω_S stand for the resonant frequencies of the anti-symmetric and symmetric with respect to C_2-symmetry modes in the bi-layer metasurface. Eq. (S28) shows that the anti-symmetric mode corresponds to the eigenvector $(1, 1)^T$ (note that the modes have opposite classifications with respect to the broken horizontal mirror symmetry). Thus, in the anti-symmetric hybrid mode, the resonances of the top and bottom metasurfaces are excited with the same amplitudes and phases.

Although one can try to evaluate this Hamiltonian in the near-field and intermediate regimes considering only far fields according to Eq. (S23), this approach will be incorrect, as the resonances are mostly coupled through near fields. To prove this statement, we calculate the resonant frequencies of the coupled modes in the stacked metasurfaces without notches (see Supplementary Fig. 3a). The dependence of the resonant frequencies on the interlayer distance is very similar to that in the structure with notches; nevertheless, here we observe coupling between two BIC modes into their symmetric and anti-symmetric hybrids, which are also optically inactive at normal incidence due to high symmetry of the structure. Henceforth, the near fields play a primary role in the formation of the resonant energies. Interestingly, the near-field coupling of two BIC resonances that exhibit nonzero intrinsic losses can lead to the formation of exceptional points.[14]

However, when calculating the far-field components of resonant input and output vectors, the necessity to consider the near fields can be relaxed as the single-layer metasurfaces weakly scatter far-fields with resonance-mismatching polarization into near fields. One can see that the near-fields weakly perturb the field profile of the incoming and scattered plane waves when a single-layer metasurface is illuminated by a wave of mismatching polarization

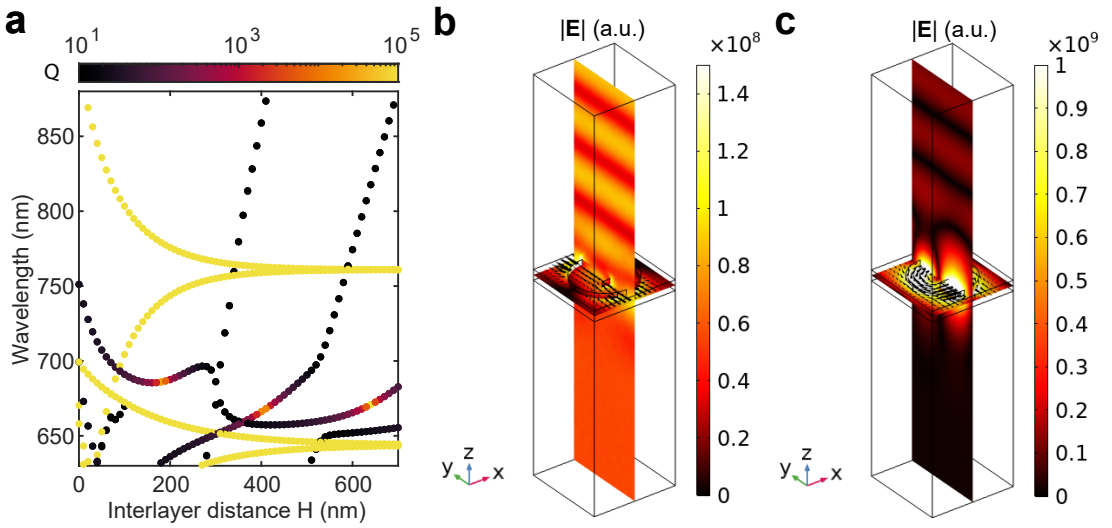

Supplementary Fig. 3: Role of the near-fields in the resonant mode coupling. **a,** Frequency of the hybridized resonant modes in the bi-layer metasurface comprising aligned discs without notches as a function of interlayer distance H. The color represents the Q-factor of the resonant modes; the color bar limits are manually set to 10 and 10^5. **b,c,** Electric fields excited in a notched single-layer metasurface by y-polarized (the resonance is decoupled) and x-polarized (the resonance is excited) plane waves at 726 nm.

(Supplementary Fig. 3b). Note that it is not the case when the resonance is excited by a wave with proper polarization (Supplementary Fig. 3c), which is also the reason why we do not calculate the coupling Hamiltonian in the far-field approximation. The resonant input and output vectors of a stacked structure in the general case were derived in Refs.,[12,13] they are given as:

$$\langle I^{\mathrm{c}}| = X^{-1}\begin{pmatrix} \langle I_d^{\mathrm{a}}| + \langle I_u^{\mathrm{a}}|\,\mathcal{P}\tilde{\mathrm{S}}_{ud}^{\mathrm{b}}\mathbb{D}_{dd}\mathcal{P}\tilde{\mathrm{S}}_{dd}^{\mathrm{a}} & \langle I_u^{\mathrm{a}}|\,\mathbb{D}_{uu}\mathcal{P}\tilde{\mathrm{S}}_{uu}^{\mathrm{b}} \\ \langle I_d^{\mathrm{b}}|\,\mathbb{D}_{dd}\mathcal{P}\tilde{\mathrm{S}}_{dd}^{\mathrm{a}} & \langle I_u^{\mathrm{b}}| + \langle I_d^{\mathrm{b}}|\,\mathcal{P}\tilde{\mathrm{S}}_{du}^{\mathrm{a}}\mathbb{D}_{uu}\mathcal{P}\tilde{\mathrm{S}}_{uu}^{\mathrm{b}} \end{pmatrix}, \tag{S29}$$

$$|O^{\mathrm{c}}\rangle = \begin{pmatrix} |O_u^{\mathrm{a}}\rangle + \tilde{\mathrm{S}}_{uu}^{\mathrm{a}}\mathcal{P}\tilde{\mathrm{S}}_{ud}^{\mathrm{b}}\mathbb{D}_{dd}\mathcal{P}\,|O_d^{\mathrm{a}}\rangle & \tilde{\mathrm{S}}_{uu}^{\mathrm{a}}\mathbb{D}_{uu}\mathcal{P}\,|O_u^{\mathrm{b}}\rangle \\ \tilde{\mathrm{S}}_{dd}^{\mathrm{b}}\mathbb{D}_{dd}\mathcal{P}\,|O_d^{\mathrm{a}}\rangle & |O_d^{\mathrm{b}}\rangle + \tilde{\mathrm{S}}_{dd}^{\mathrm{b}}\mathcal{P}\tilde{\mathrm{S}}_{du}^{\mathrm{a}}\mathbb{D}_{uu}\mathcal{P}\,|O_u^{\mathrm{b}}\rangle \end{pmatrix} X. \tag{S30}$$

Here, X is the matrix of eigenvectors of the coupling Hamiltonian derived in Eq. (S28). Due to weak background scattering of the far-fields to near-fields, we can omit the near-fields when writing the background scattering matrices $\tilde{\mathrm{S}}$ in Eqs. (S29), (S30) and use Eq. (S23)

to write down the resonant input vectors of the coupled modes as:

$$\langle I^{c}| = \begin{pmatrix} \langle I_A^{c}| \\ \langle I_S^{c}| \end{pmatrix} = \tag{S31}$$

$$= \underbrace{\begin{pmatrix} 0.5 & 0.5 \\ 0.5 & -0.5 \end{pmatrix}}_{X^{-1}} \begin{pmatrix} A\left(\cos\theta,\, -\sin\theta\right)\left(1+\dfrac{e^{-2i\phi}rt}{1-r^2e^{-2i\phi}}\right) & A\left(\cos\theta,\, -\sin\theta\right)\dfrac{e^{-i\phi}t}{1-r^2e^{-2i\phi}} \\ A\left(\cos\theta,\, \sin\theta\right)\dfrac{e^{-i\phi}t}{1-r^2e^{-2i\phi}} & A\left(\cos\theta,\, \sin\theta\right)\left(1+\dfrac{e^{-2i\phi}rt}{1-r^2e^{-2i\phi}}\right) \end{pmatrix}.$$

Here, $\langle I_A^{c}|$ and $\langle I_S^{c}|$ are the resonant input vectors of the anti-symmetric and symmetric hybridized resonances. For example, the explicit form of the resonant input vector of the anti-symmetric mode appears as:

$$\langle I_A^{c}| = \frac{A}{2}\begin{pmatrix} \cos\theta\left(1+\dfrac{e^{-2i\phi}rt+e^{-i\phi}t}{1-r^2e^{-2i\phi}}\right) \\ -\sin\theta\left(1+\dfrac{e^{-2i\phi}rt-e^{-i\phi}t}{1-r^2e^{-2i\phi}}\right) \\ \cos\theta\left(1+\dfrac{e^{-2i\phi}rt+e^{-i\phi}t}{1-r^2e^{-2i\phi}}\right) \\ \sin\theta\left(1+\dfrac{e^{-2i\phi}rt-e^{-i\phi}t}{1-r^2e^{-2i\phi}}\right) \end{pmatrix}^{T}. \tag{S32}$$

Now when the bi-layer metasurface is excited by normally incident RCP or LCP plane waves from the top, the amplitudes of the incoming waves are given as:

$$\mathcal{A}_{in}^{R,L} = \left(1,\, \pm i,\, 0,\, 0\right)^{T}. \tag{S33}$$

Using the resonant input vectors $\langle I_A^{c}|$ from Eq. (S32), we write the excited amplitudes of the anti-symmetric resonance as a product of the resonant input vector and the incoming wave amplitudes:

$$\alpha^{R,L} \propto \langle I_A^{c}|\, \mathcal{A}_{in}^{R,L} \propto$$
$$\left(\cos\theta \mp i\sin\theta\right) + \left(\cos\theta \mp i\sin\theta\right)\frac{e^{-2i\phi}rt}{1-r^2e^{-2i\phi}} + \left(\cos\theta \pm i\sin\theta\right)\frac{e^{-i\phi}t}{1-r^2e^{-2i\phi}}, \tag{S34}$$

with $\phi = nk_0H$. The three terms in Eq. (S34) have clear physical meanings. The first term represents the direct coupling of the upper metasurface resonance to the plane wave coming from the top. The second term is the coupling of the upper metasurface resonance from the bottom to the wave that was transmitted through the upper metasurface with the coefficient t, gained a factor $e^{-i\phi}$ while propagating through the separation layer, then was reflected from the lower metasurface with coefficient r, and then propagated back acquiring the factor $e^{-i\phi}$ one more time. The Fabry-Pérot denominator $(1 - r^2e^{-2i\phi})$ in the second term takes into account the infinite number of nonresonant reflections that happened while the wave was bouncing back and forth between the metasurfaces. The third term stands for the coupling of the lower metasurface resonance to the wave that passed through the upper metasurface and the intermediate layer undergoing all the reflections of the Fabry-Pérot type. To highlight the direct correspondence between the dipole coupling model and the TCMT for stacked resonant structures we compare the resonant amplitudes calculated using Eqs. (S18) and (S34). The two approaches are equivalent if Eqs. (S9) and (S10) hold, thus TCMT leads us to the same system of equations Eqs. (S16), (S19) that defines H and θ of absolutely chiral bi-layer metasurface.

For example, under the first chirality condition for the anti-symmetric mode

$$re^{-ink_0H} = |r|, \quad \pm\tan\theta = |t|/(1-|r|) \tag{S35}$$

Eq. (S32) transforms into:

$$\langle I_A^{\mathrm{c}}| = \frac{A}{2}\begin{pmatrix} \cos\theta\left(1+\dfrac{i|t|}{1-|r|}\right) \\ -\sin\theta\left(1-\dfrac{i|t|}{1+|r|}\right) \\ \cos\theta\left(1+\dfrac{i|t|}{1-|r|}\right) \\ \sin\theta\left(1-\dfrac{i|t|}{1+|r|}\right) \end{pmatrix}^T = \frac{A}{2}\cos\theta\left(1+i\frac{1+|r|}{|t|}\right)\begin{pmatrix} 1 \\ \pm i \\ 1 \\ \mp i \end{pmatrix}^T \tag{S36}$$

Similar relations can be derived for the case of plane wave excitation from the bottom; the only difference is the sign change in front of $\sin\theta$ in Eq. (S32). At the same time, amplitudes of RCP and LCP waves are defined as $(0, 0, 1, \mp i)$ respectively due to the inverted propagation direction; thus, the chiral resonance couples to the waves of the same helicity regardless of the excitation side.

It is also illustrative to derive the resonant output vectors $\left|O^{\mathrm{c}}_{A,S}\right\rangle$ in Eq. (S30) in the far-field approximation:

$$|O^{\mathrm{c}}\rangle = \begin{pmatrix} |O^{\mathrm{c}}_A\rangle & |O^{\mathrm{c}}_S\rangle \end{pmatrix} = \tag{S37}$$

$$= \begin{pmatrix} A\begin{pmatrix}\cos\theta\\ -\sin\theta\end{pmatrix}\left(1+\frac{e^{-2i\phi}rt}{1-r^2e^{-2i\phi}}\right) & A\begin{pmatrix}\cos\theta\\ \sin\theta\end{pmatrix}\frac{e^{-i\phi}t}{1-r^2e^{-2i\phi}} \\ A\begin{pmatrix}\cos\theta\\ -\sin\theta\end{pmatrix}\frac{e^{-i\phi}t}{1-r^2e^{-2i\phi}} & A\begin{pmatrix}\cos\theta\\ \sin\theta\end{pmatrix}\left(1+\frac{e^{-2i\phi}rt}{1-r^2e^{-2i\phi}}\right) \end{pmatrix} \underbrace{\begin{pmatrix} 1 & 1 \\ 1 & -1 \end{pmatrix}}_{X}.$$

For example, using the same chirality condition in Eq. (S35), we obtain the explicit form of the anti-symmetric resonance output vector:

$$|O^{\mathrm{c}}_A\rangle = A\begin{pmatrix} \cos\theta\left(1+\frac{i|t|}{1-|r|}\right) \\ -\sin\theta\left(1-\frac{i|t|}{1+|r|}\right) \\ \cos\theta\left(1+\frac{i|t|}{1-|r|}\right) \\ \sin\theta\left(1-\frac{i|t|}{1+|r|}\right) \end{pmatrix} = A\cos\theta\left(1+i\frac{1+|r|}{|t|}\right)\begin{pmatrix} 1 \\ \pm i \\ 1 \\ \mp i \end{pmatrix}. \tag{S38}$$

Eqs. (S36) and (S38) show that the chiral resonance that can be excited by RCP (LCP) waves emits RCP (LCP) waves into the top and bottom directions. Consequently, the resonance appears to be entirely decoupled from the waves of the mismatched polarization. The resonance can neither be excited by such waves nor radiates them. Thus, the bi-layer metasurface with intrinsically chiral resonance behaves as a chiral mirror. The same result can be demonstrated for the second chirality condition.

Supplementary Note 5. Comparison of the embedded and open structures for intrinsic chirality

As was mentioned in the main text, the near-field coupling regime can be preferred due to the strong interaction between the resonant modes of the top and bottom metasurfaces which even allows for achieving chirality in a bi-layer structure of different metasurfaces. In Supplementary Fig. 4, we compare the resonant modes of the fully embedded structure (varied H and θ, all other parameters as in the configuration A2) and the "open" structure with the top discs surrounded by air (varied H and θ, all other parameters as in the configuration A1). While the two lowest modes of the fully embedded structure converge in frequency at large interlayer distances H, it does not happen in the case of the "open" structure because the modes of isolated top and bottom metasurfaces have different resonant frequencies. Accordingly, the open structure is not capable of demonstrating chirality at $H > 200$ nm as the lowest-frequency mode of the structure mainly consists of the lowest-frequency mode of the bottom fully embedded disc. Nevertheless, for H values close to 60 nm, the interlayer near-field coupling is sufficient to sustain modes of both top and bottom metasurfaces to achieve intrinsic chirality.

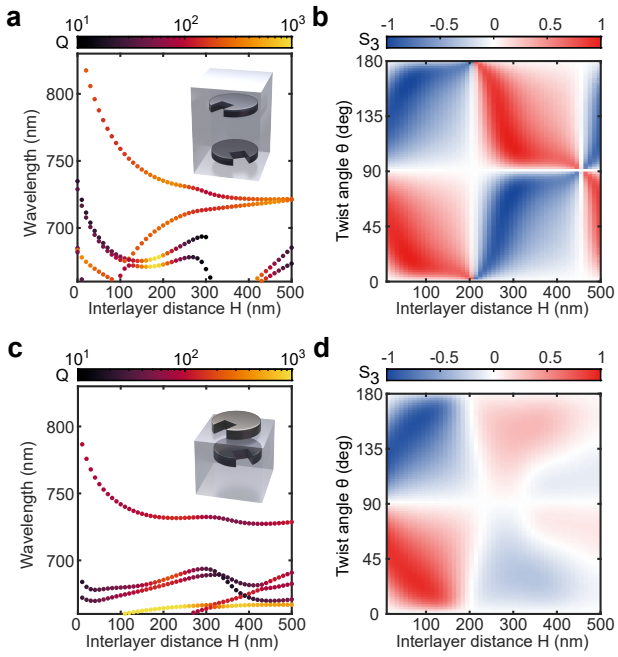

Supplementary Fig. 4: Comparison of the embedded and open structures. **a,c,** Resonant energies of the coupled modes in the embedded and open bi-layer metasurfaces in dependence on the interlayer distance. **b,d,** Resonance chirality of the lowest-frequency mode of the embedded and open bi-layer metasurfaces with varied twist angle θ and interlayer distance H.

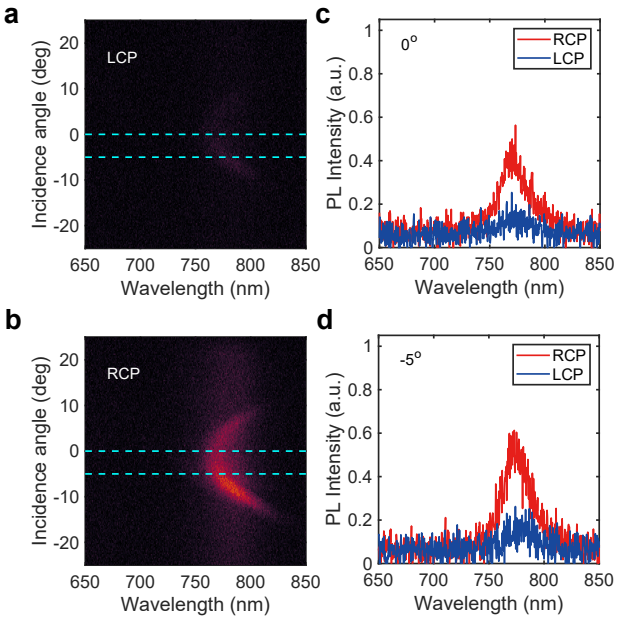

Supplementary Fig. 5: Chiral emission from bi-layer metasurface A1 with perfect alignment (zero lateral displacement) along x direction. **a, b,** Measured angle-resolved spectra of the LCP and RCP photoluminescence emission. **c, d,** Emission spectra at 0° and -5° emission angles.

Supplementary Note 6. Reflectance spectra for bi-layer metasurfaces operating at unitary background transmission of the Fabry-Pérot type.

In this section, we select three interlayer distances $H = 50$ nm (Supplementary Fig. 6), 280 nm (Supplementary Fig. 7), and 530 nm (Supplementary Fig. 8) at which the optimal chirality can be achieved and calculate the reflectance spectra for various twist angles θ to illustrate the possibilities of polarization control. Note that active chirality switching due to relative rotation of the whole metasurfaces by an angle $2\Delta\theta = 90^o$ is possible for structures operating in the near-field coupling regime $H = 50$ nm ($\theta = 20^o \Rightarrow \theta = 155^o = -25^o$) and intermediate coupling regime $H = 280$ nm ($\theta = 45^o \Rightarrow \theta = 90^o \Rightarrow \theta = 135^o$). The resonances spectrally overlap for the structures with $H > 500$ nm and cannot be used for chirality switching. Also, Supplementary Fig. 7d demonstrates the absolute chirality of the symmetric mode for the structure operating in the intermediate regime with the model parameters corresponding to configuration A2 from the main text. The calculated reflectance spectra agree well with the experimentally measured spectra shown in Fig. 3i of the main text.

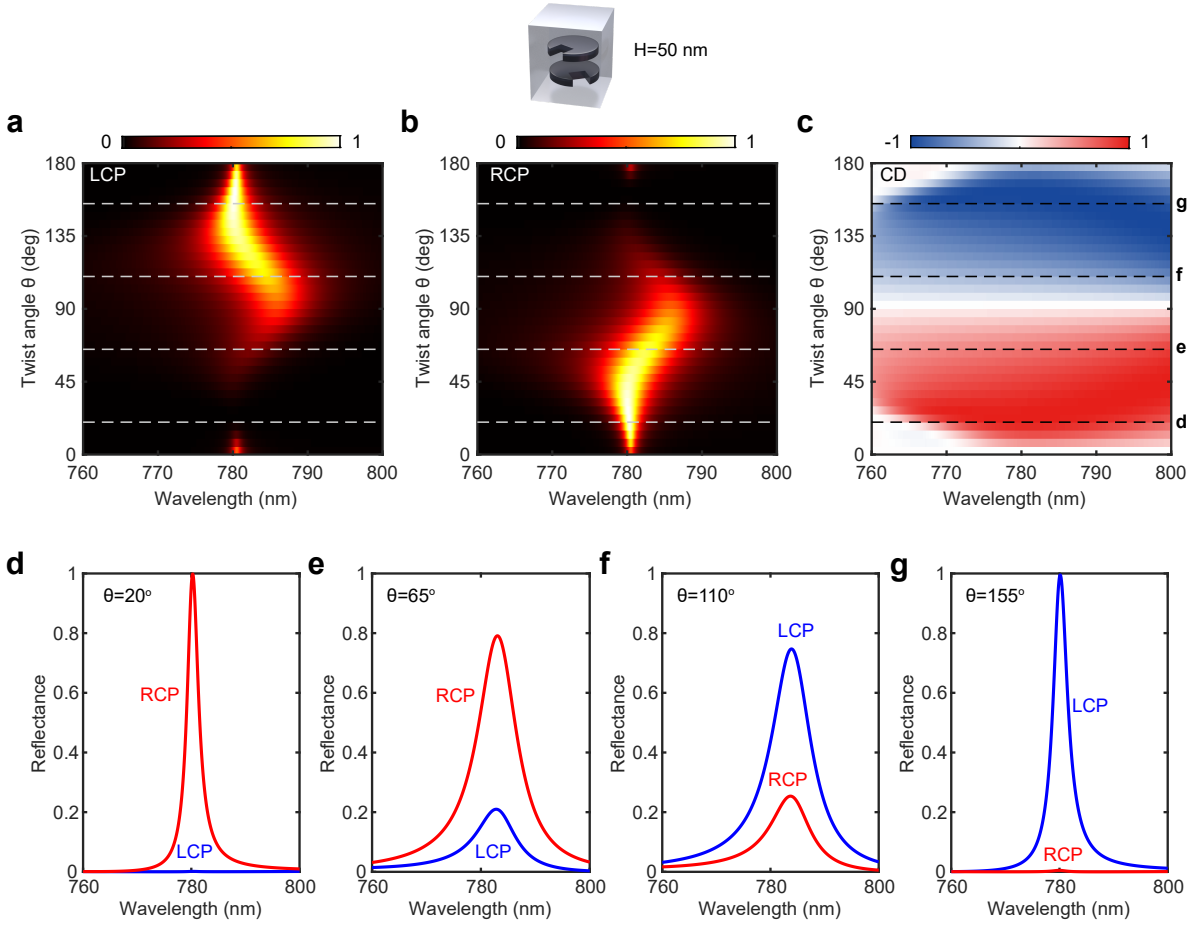

Supplementary Fig. 6: Bi-layer metasurface in near-field coupling regime with $H = 50$ nm. **a,b,** Simulated LCP and RCP reflection spectra at normal incidence of the bi-layer metasurface with variable twist angle θ. **c,** CD spectra calculated based on **a** and **b**. **d-g,** Reflectance spectra for metasurfaces with selected twist angles θ.

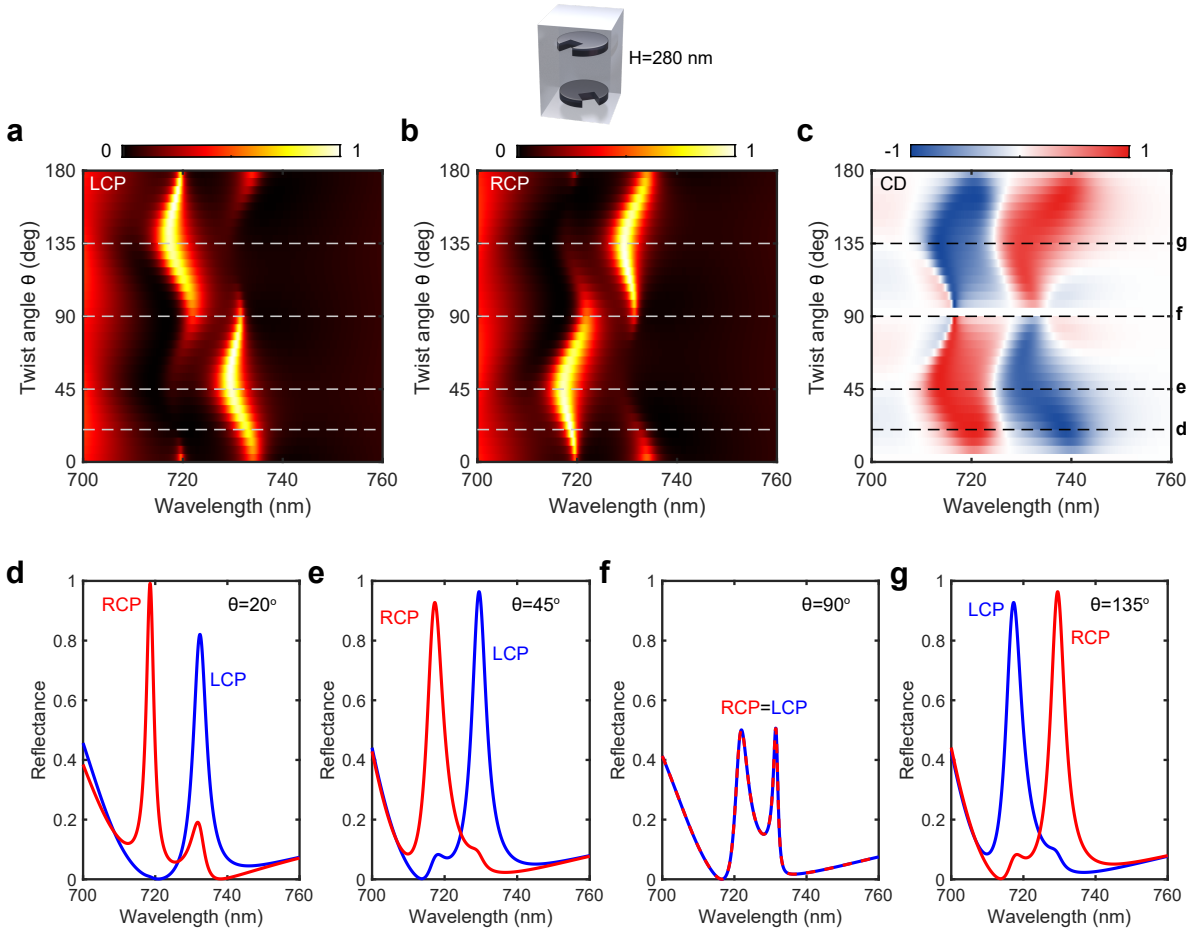

Supplementary Fig. 7: Bi-layer metasurface in intermediate coupling regime with $H = 280$ nm. **a,b,** Simulated LCP and RCP reflection spectra at normal incidence of the bi-layer metasurface with variable twist angle θ. **c,** CD spectra calculated based on **a** and **b**. **d-g,** Reflectance spectra for metasurfaces with selected twist angles θ.

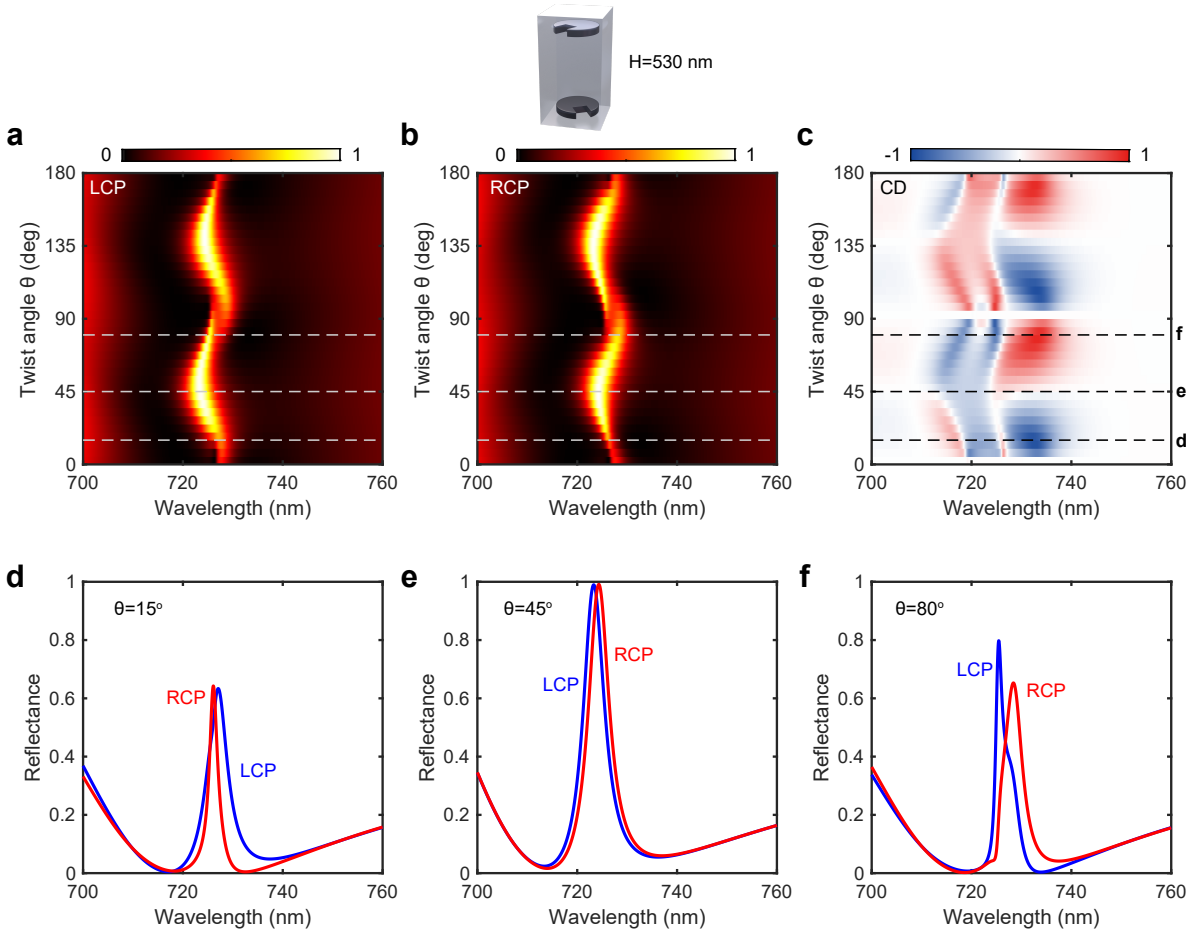

Supplementary Fig. 8: Bi-layer metasurface in far-field coupling regime with $H = 530$ nm. **a,b,** Simulated LCP and RCP reflection spectra at normal incidence of the bi-layer metasurface with variable twist angle θ. **c,** CD spectra calculated based on **a** and **b**. **d-f,** Reflectance spectra for metasurfaces with selected twist angles θ.

Let us examine the possibility of achieving maximum chirality in the purely far-field regime. At large H we can analytically evaluate the effective coupling Hamiltonian (S26) while neglecting near-field coupling. Using $A^2 = i\gamma(r+t)$ (see[8]), in the far-field approximation, it reads:

$$H = \begin{pmatrix} \Omega + i\gamma + \dfrac{i\gamma e^{2i(\Phi-\phi)}|r|(|r|+i|t|)}{1-|r|^2e^{2i(\Phi-\phi)}} & \cos(2\theta)\dfrac{i\gamma e^{i(\Phi-\phi)}(|r|+i|t|)}{1-|r|^2e^{2i(\Phi-\phi)}} \\ \cos(2\theta)\dfrac{i\gamma e^{i(\Phi-\phi)}(|r|+i|t|)}{1-|r|^2e^{2i(\Phi-\phi)}} & \Omega + i\gamma + \dfrac{i\gamma e^{2i(\Phi-\phi)}|r|(|r|+i|t|)}{1-|r|^2e^{2i(\Phi-\phi)}} \end{pmatrix}, \tag{S39}$$

where we explicitly write the real and imaginary part of the single-layer resonant frequencies $\omega_1^{\mathrm{a,b}} = \Omega + i\gamma$, while the reflection phase Φ and propagation phase ϕ were defined in (S11) and (S25). Since maximum chirality can only be achieved at the background Fabry-Pérot resonance (S16), we put $e^{i(\Phi-\phi)} = \pm 1$. The resonant energies of the purely far-field coupled modes are eigenvalues of the Hamiltonian:

$$\omega_{A,S} = \omega - \frac{|r||t|}{1-|r|^2} + i\frac{\gamma}{1-|r|^2} \pm \cos(2\theta)\frac{\gamma|t|}{1-|r|^2} \mp i\cos(2\theta)\frac{\gamma|r|}{1-|r|^2} \tag{S40}$$

Thus, the spectral separation of the resonant modes is equal to $\cos(2\theta)\dfrac{2\gamma|t|}{1-|r|^2}$, while the imaginary parts of the resonant modes are equal $\mathrm{Im}(\omega_{A,S}) = \dfrac{\gamma}{1-|r|^2}(1\mp|r|\cos(2\theta))$. We note that $\mathrm{Im}(\omega_A) + \mathrm{Im}(\omega_S) = \dfrac{2\gamma}{1-|r|^2} > \cos(2\theta)\dfrac{2\gamma|t|}{1-|r|^2}$, hence, the tails of the resonant modes overlap anyways. Moreover, chirality condition for the angle θ (S19) results in $\cos(2\theta) = \pm|r|$, hence two chiral modes have imaginary parts γ and $\gamma\dfrac{1+|r|^2}{1-|r|^2}$. The spectral separation of the chiral modes $\dfrac{2\gamma|t||r|}{1-|r|^2} = \dfrac{2\gamma|r|}{|t|}$ turns out to be smaller than the imaginary part of the broader mode, which means that the broader resonance will always interfere with the sharper resonance. However, we note that for significantly large $|r|$ the imaginary part of the broader mode can be much larger than that of the sharper mode, which means that the latter can dominate in a narrow spectral region. Still, designs with large separation distances and $|r|$ close to 1 appear impractical since the Fabry-Pérot factor $1/(1-r^2\exp(-nk_0H))$ rapidly

oscillates with frequency in this case.

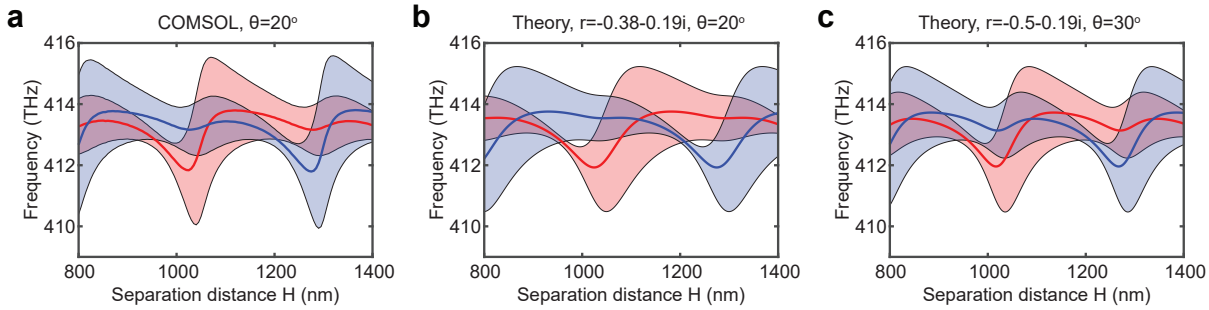

Supplementary Fig. 9: Comparison of the resonant frequencies of bi-layer metasurfaces **a,** simulated using COMSOL and calculated as eigenvalues of the coupling Hamiltonian in the far-field approximation with **b,** $r = -0.38 - 0.19i$, and $\theta = 20°$ and **c,** $r = -0.5 - 0.19i$, and $\theta = 30°$. Solid lines indicate the real part of the resonant frequencies $\mathrm{Re}(\omega_{A,S})$, the shaded areas indicate $\pm\mathrm{Im}(\omega_{A,S})$.

To corroborate the validity of the far-field approach, we simulated the resonant frequencies of bi-layer metasurfaces with $\theta = 20°$ and $H > 800$ nm using the COMSOL eigenmode solver (Supplementary Fig. 9a). Then, we compared them to the analytical results given by (S39), where we used $\Omega = 413.2$ THz, $\gamma = 0.9$ THz, $r = -0.38 - 0.19i$, and $\theta = 20°$ (Supplementary Fig. 9b). Although the theoretical model well reproduces the simulation result, an even better agreement is achieved for $r = -0.5 - 0.19i$, and $\theta = 30°$ (Supplementary Fig. 9c), which is easily explained by the subtle anisotropy of the reflection coefficient r and the slight deviation of the effective dipole from the approximation $\mathbf{D}(\theta) \propto (\cos\theta, \sin\theta)$.

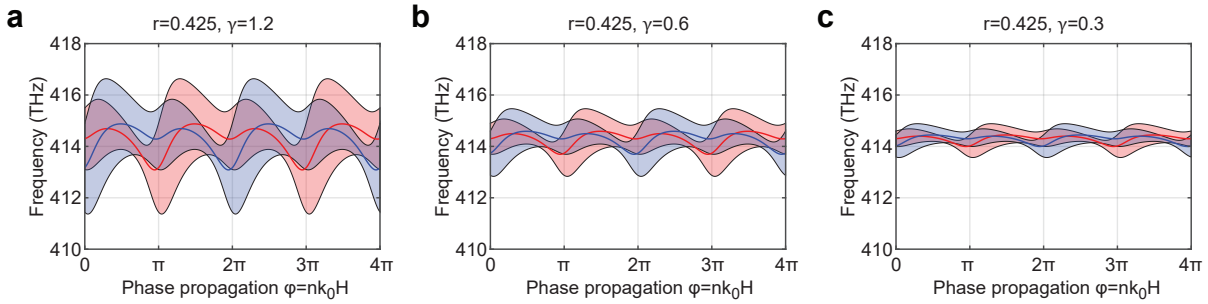

Supplementary Fig. 10: Resonant frequencies of bi-layer metasurfaces calculated as eigenvalues of the coupling Hamiltonian in the far-field approximation with **a,** $\gamma = 1.2$ **b,** $\gamma = 0.6$ **c,** $\gamma = 0.3$.

Next, for simplicity, we assume $r = 0.425$ and $\tan\theta = |t|/(1 + |r|)$. As shown in Supple-

mentary Fig. 10, variation of the imaginary part γ (*i.e.*, radiative losses of the resonance) does not allow for the separation of modes, since the coupling strength (*i.e.*, off-diagonal elements of the coupling Hamiltonian) is directly proportional to γ.

Finally, by increasing the magnitude of background reflection $|r|$ we can achieve significant oscillation of the resonant frequencies (see Supplementary Fig. 11), however, the modes strongly overlap at the Fabry-Pérot resonances.

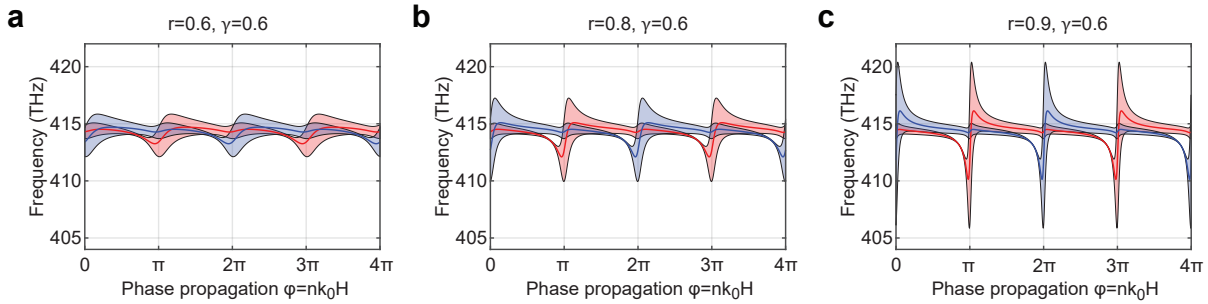

Supplementary Fig. 11: Resonant frequencies of bi-layer metasurfaces calculated as eigenvalues of the coupling Hamiltonian in the far-field approximation with **a,** $r = 0.6$ **b,** $r = 0.8$ **c,** $r = 0.9$.

Supplementary Note 7. Unidirectional resonances in bi-layer metasurfaces with lateral displacement

At each point in the reciprocal space, the total radiative losses of the resonance can be represented as a sum of losses in the top and bottom half-spaces: $\gamma_r = \gamma_{top} + \gamma_{bot}$. The radiative losses are related to the radiative Q-factor of the resonance $Q = \omega/2\gamma_r$ (Supplementary Fig. 12b), which can be extracted from the eigenmode simulation of a nonglossy metasurface. At the same time, the radiative losses are proportional to the squared absolute value of the far-field amplitude of the resonant mode, which we illustrate in Fig. 1e of the main text and Supplementary Fig. 13. At the same time, a unidirectional resonance exhibits large radiation asymmetry in the up-down direction (Supplementary Fig. 12c), which is $\gamma_{top}/\gamma_{bot} \ll 1$ or $\gamma_{top}/\gamma_{bot} \gg 1$.

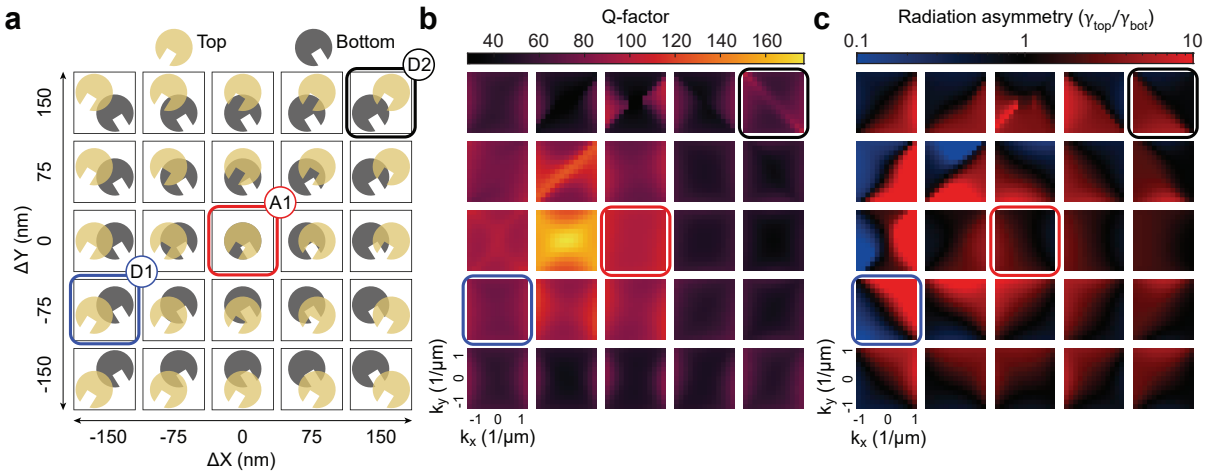

Supplementary Fig. 12: **a,** Unit cell (top view) of bi-layer metasurfaces with possible lateral shifts ranging from -150 nm to 150 nm in both directions. **b, c,** Corresponding maps of Q-factor and up-down radiation asymmetry $\gamma_{top}/\gamma_{bot}$ for the anti-symmetric (lowest) resonant mode.

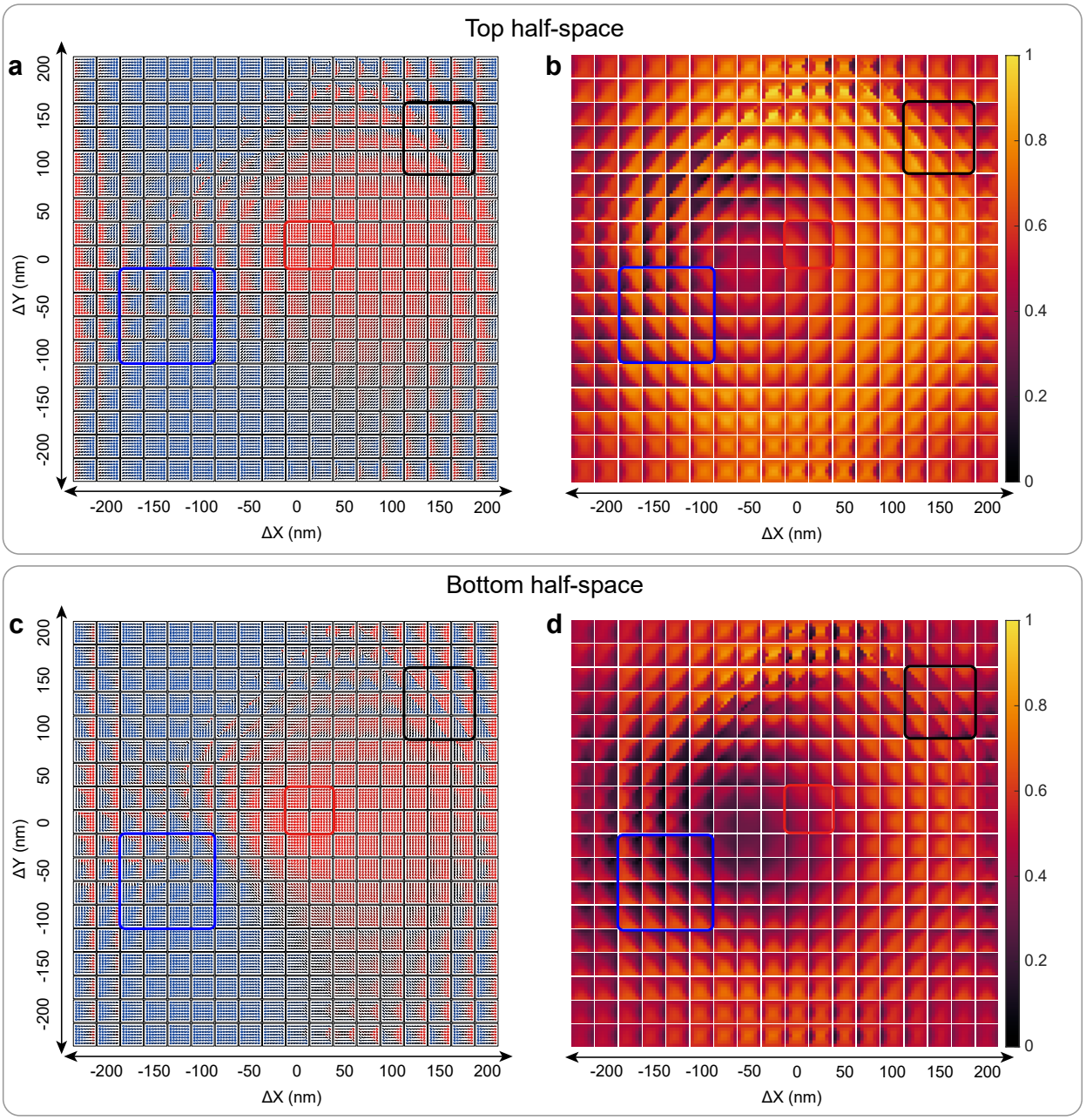

Supplementary Fig. 13: Maps of **a,c,** eigenpolarization and **b,d,** far-field amplitude in the top and bottom half-spaces for the anti-symmetric (lowest) resonant mode in the reciprocal space, where k_x and k_y values range from -1 μm^{-1} to 1 μm^{-1}.

Supplementary Note 8. Extrinsic chirality of configuration D2

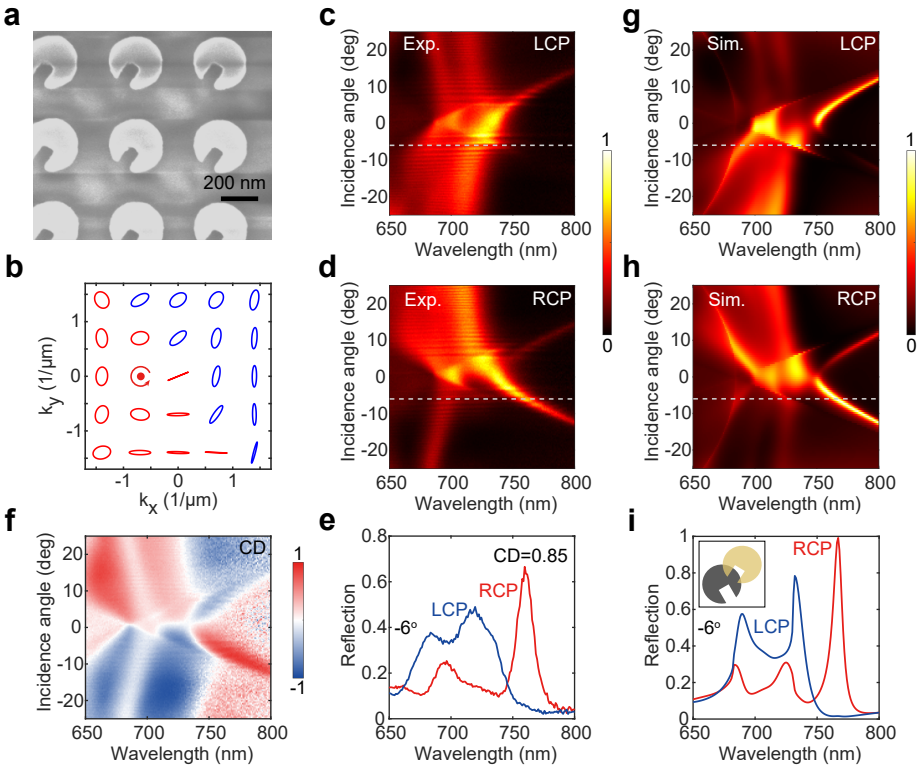

Supplementary Fig. 14: Reflection properties of bi-layer metasurface D2 with extrinsic chirality. **a,** SEM image of the bi-layer twisted metasurface with the designed lateral displacement $\Delta X = 180$ nm, $\Delta Y = 120$ nm. **b,** Calculated eigenpolarization map of the anti-symmetric resonance. **c, d,** Measured angle-resolved reflection spectra under LCP and RCP illumination. **e,** Measured reflection spectra at 6 degrees incidence corresponding to the dashed lines in **c** and **d**. **f,** Angle-resolved circular dichroism extracted from the reflection spectra in **c**, **d**. **g-i**, Simulated reflection spectra corresponding to **c-e**.

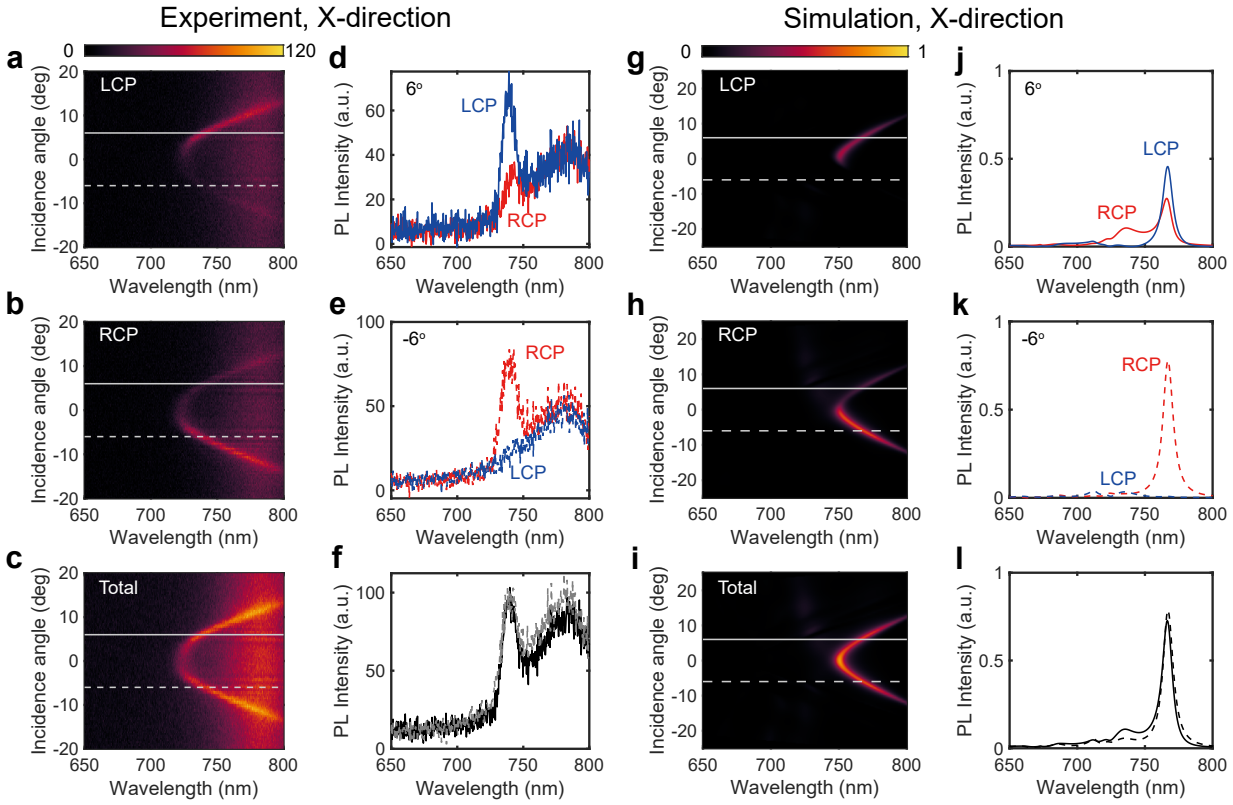

Supplementary Fig. 15: Chiral emission from bi-layer metasurface D2 with lateral displacement $\Delta X = 180$ nm, $\Delta Y = 120$ nm along x direction. **a, b, c,** Measured, and **g, h, i** simulated angle-resolved spectra of the LCP, RCP, and total intensity of the photoluminescence emission. **d, e, f,** Measured, and **j, k, l,** simulated spectra of the LCP, RCP, and total intensity of the emission at $\pm 6^o$ emission angle. The corresponding angles are denoted with solid and dashed lines in panels **a, b, c,** and **g, h, i**.

Supplementary Note 9. Unidirectional chiral emission from configuration D1

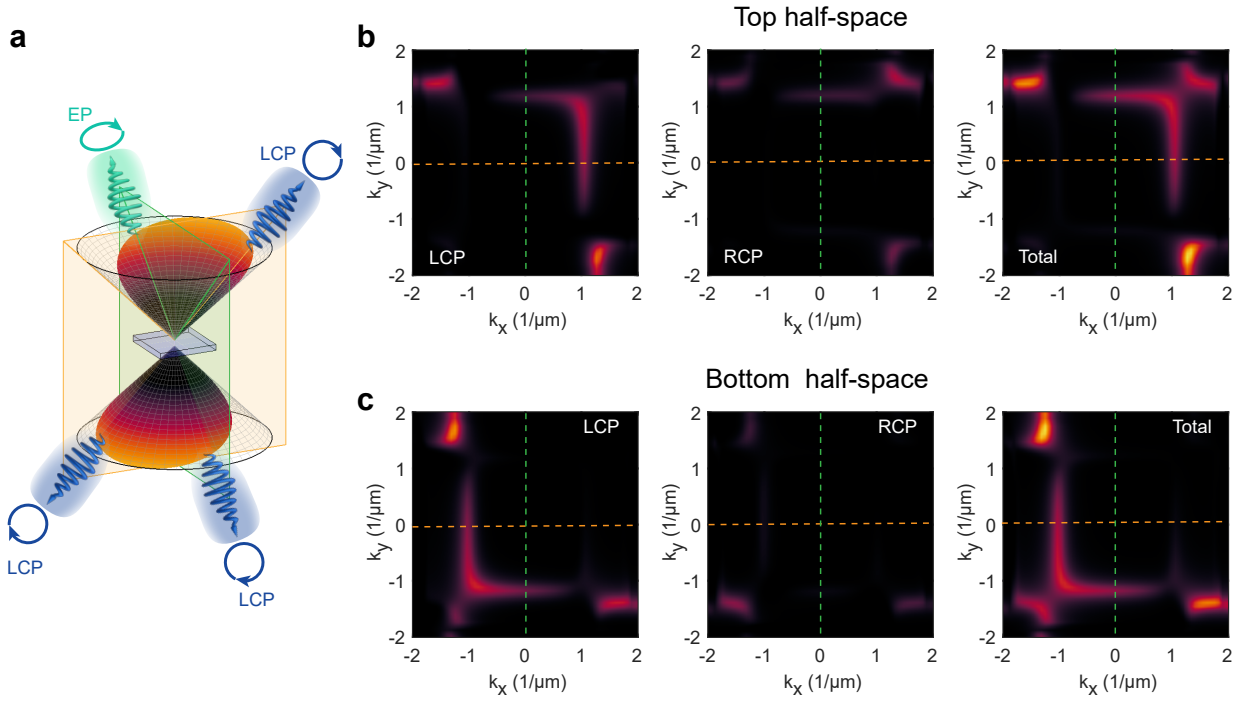

Supplementary Fig. 16: Calculated emission intensity in the top and bottom half-spaces from bi-layer metasurface D1 with lateral displacement $\Delta X = -150$ nm, $\Delta Y = -75$ nm at wavelength 770 nm.

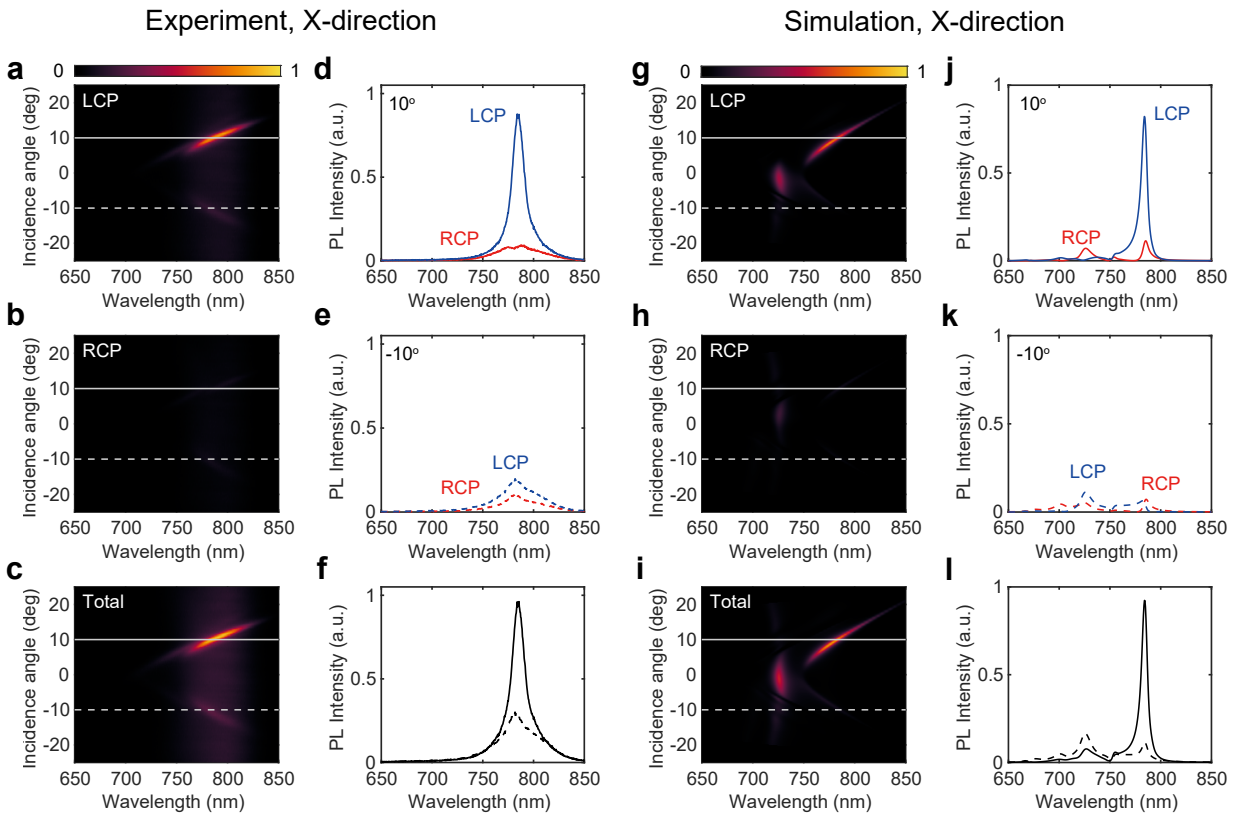

Supplementary Fig. 17: Unidirectional chiral emission from bi-layer metasurface D1 with lateral displacement $\Delta X = -150$ nm, $\Delta Y = -75$ nm along x direction. **a, b, c,** Measured, and **g, h, i** simulated angle-resolved spectra of the LCP, RCP, and total intensity of the photoluminescence emission. **d, e, f,** Measured, and **j, k, l,** simulated spectra of the LCP, RCP, and total intensity of the emission at $\pm 10^o$ emission angle. The corresponding angles are denoted with solid and dashed lines in panels **a, b, c,** and **g, h, i**.

Supplementary Methods 1. Fabrication

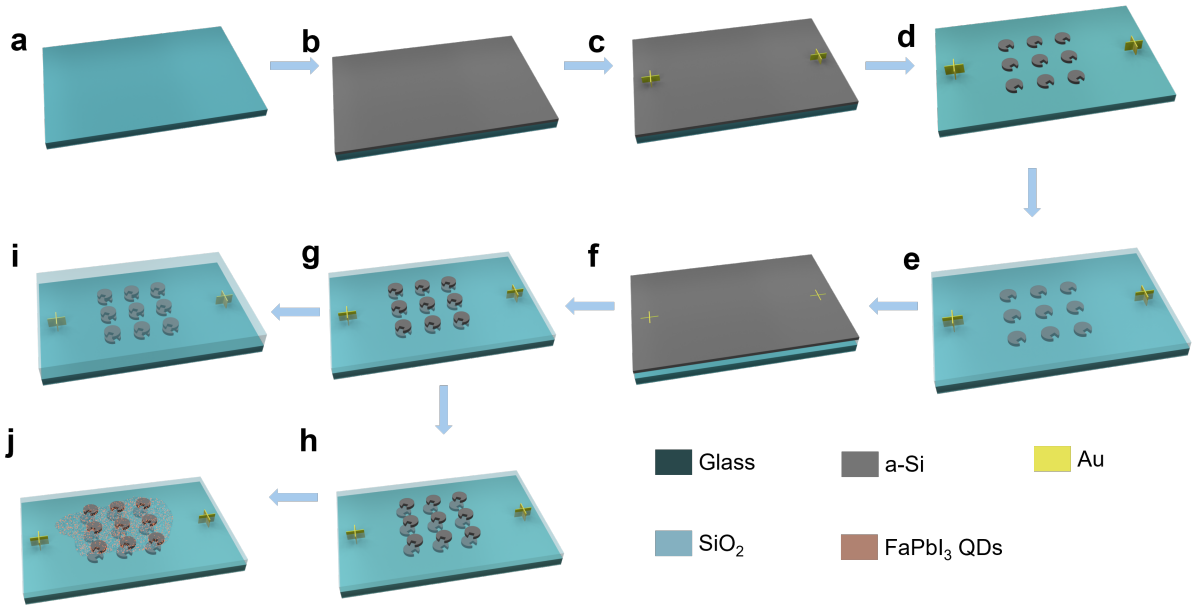

Supplementary Fig. 18: Schematic illustration of the bi-layer metasurface fabrication process. **a,** Clean glass substrate for later fabrication process. **b,** Growth of a-Si layer on the glass substrate to prepare for bottom Si disks. **c,** Au alignment markers are made by EBL, evaporation, and lift-off. **d,** Bottom Si disks are fabricated by EBL and etching. **e,** Formation of middle SiO_2 layer by spin coating and etching. **f,** Deposition of a-Si layer. **g,** Formation of well-aligned and **h** displaced top Si disks. **i,** Fabrication of an embedded structure by incorporation of another SiO_2 layer. **j,** Deposition of emitters on the open structure by drop casting.

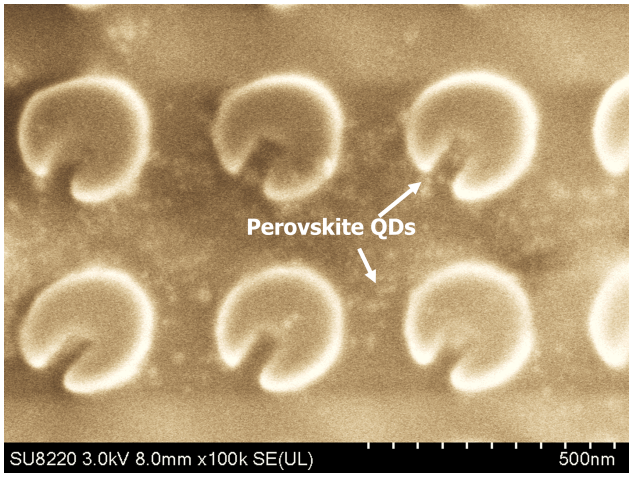

Supplementary Fig. 19: SEM image of the bi-layer metasurface, top layer with deposited perovskite quantum dot emitters.

Supplementary Methods 2. Optical setup

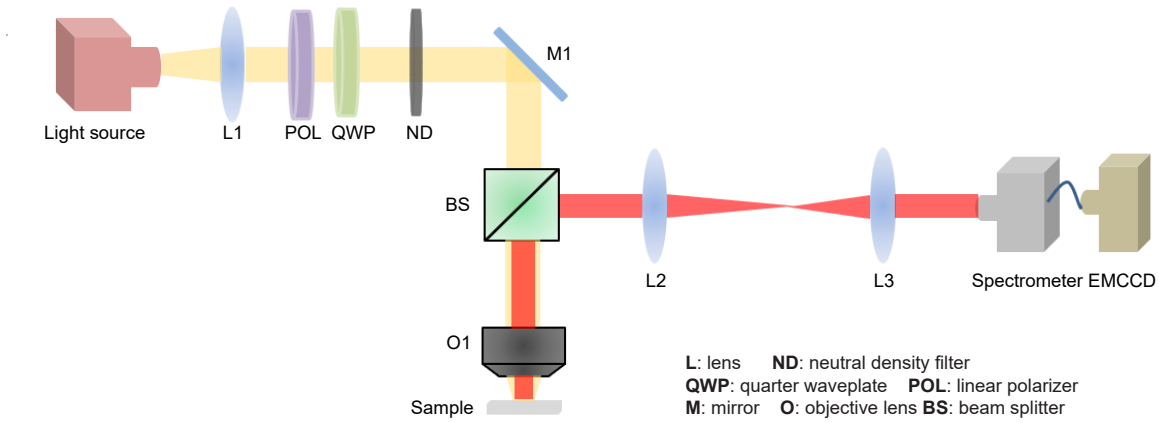

Supplementary Fig. 20: Optical setup for the characterization of the reflectance spectra.

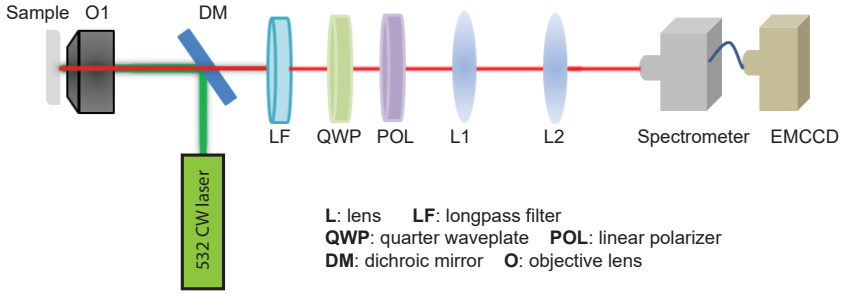

Supplementary Fig. 21: Optical setup for the characterization of the photoluminescence.

References

(1) Doost, M. B.; Langbein, W.; Muljarov, E. A. Resonant-state expansion applied to three-dimensional open optical systems. *Phys. Rev. A* **2014**, *90*, 013834.

(2) Muljarov, E. A.; Weiss, T. Resonant-state expansion for open optical systems: generalization to magnetic, chiral, and bi-anisotropic materials. *Optics letters* **2018**, *43*, 1978–1981.

(3) Weiss, T.; Muljarov, E. A. How to calculate the pole expansion of the optical scattering matrix from the resonant states. *Physical Review B* **2018**, *98*, 085433.

(4) Lalanne, P.; Yan, W.; Vynck, K.; Sauvan, C.; Hugonin, J.-P. Light interaction with photonic and plasmonic resonances. *Laser & Photonics Reviews* **2018**, *12*, 1700113.

(5) Overvig, A. C.; Malek, S. C.; Carter, M. J.; Shrestha, S.; Yu, N. Selection rules for quasibound states in the continuum. *Physical Review B* **2020**, *102*, 035434.

(6) Cotton, F. A. *Chemical applications of group theory*; John Wiley & Sons, 1991.

(7) Saleh, B. E.; Teich, M. C. *Fundamentals of photonics*; John Wiley & Sons, 2019.

(8) Fan, S.; Suh, W.; Joannopoulos, J. D. Temporal coupled-mode theory for the Fano resonance in optical resonators. *JOSA A* **2003**, *20*, 569–572.

(9) Tikhodeev, S. G.; Yablonskii, A.; Muljarov, E.; Gippius, N. A.; Ishihara, T. Quasiguided modes and optical properties of photonic crystal slabs. *Physical Review B* **2002**, *66*, 045102.

(10) Gippius, N. A.; Weiss, T.; Tikhodeev, S. G.; Giessen, H. Resonant mode coupling of optical resonances in stacked nanostructures. *Optics Express* **2010**, *18*, 7569–7574.

(11) Weiss, T.; Gippius, N. A.; Granet, G.; Tikhodeev, S. G.; Taubert, R.; Fu, L.; Schweizer, H.; Giessen, H. Strong resonant mode coupling of Fabry–Perot and grating resonances in stacked two-layer systems. *Photonics and Nanostructures-Fundamentals and Applications* **2011**, *9*, 390–397.

(12) Gromyko, D.; Dyakov, S.; Tikhodeev, S.; Gippius, N. Resonant mode coupling approximation for calculation of optical spectra of stacked photonic crystal slabs. Part I. *Photonics and Nanostructures – Fundamentals and Applications* **2023**, *53*, 101109.

(13) Gromyko, D.; Dyakov, S.; Tikhodeev, S.; Gippius, N. Resonant mode coupling approximation for calculation of optical spectra of stacked photonic crystal slabs. Part II. *Photonics and Nanostructures – Fundamentals and Applications* **2023**, *53*, 101110.

(14) Valero, A. C.; Sztranyovszky, Z.; Muljarov, E.; Bogdanov, A.; Weiss, T. Exceptional Bound States in the Continuum. *arXiv preprint arXiv:2309.01501* **2023**,